Communications In Catalysis
Vol. 3, No. 1, 2026, pp. 33-51
DOI: 10.22049/cic.2026.32046.1044

Azarbaijan Shahid Madani University

A Novel Semi-Crystalline and Amorphous Nitrogen-Rich Phosphazene Covalent Framework for Efficient Removal of Heavy Metals from Water

Ramin Roohparvar[1, *], Mahnaz Seyyed Hejazie[2]

[1]Crop and Horticultural Research Department, East Azarbaijan Agricultural and Natural Resources 2Research and Education Center, Agricultural Research, Education and Extension Organization (AREEO), Tabriz, IRAN

[2]Former Scholar of the Ministry of Science, Research and Technology (MSRT), Tehran, IRAN

E-mail: r.roohparvar@areeo.ac.ir

Received: 2026-04-11, Accepted: 2026-04-28

Abstract: A nitrogen-rich phosphazene-based covalent framework (HM-CPF) was synthesized through microwave-assisted polycondensation of hexachlorocyclotriphosphazene and melamine for heavy metal removal from aqueous solutions. Characterization revealed semi-crystalline domains within an amorphous network, a BET surface area of 191.28 $m^2 g^{-1}$, and an average pore diameter of 10.65 nm. HM-CPF preferentially adsorbed Pb(II) and Hg(II), with Langmuir maximum capacities of 982.2 and 518.3 mg g^{-1}, respectively. Within pH 4–6, removal efficiencies exceeded 99% for Pb(II) and reached approximately 80% for Hg(II). Equilibrium data favored the Langmuir model over the Freundlich model, while adsorption kinetics followed the pseudo-second-order model. Metal affinity was attributed to coordination with nitrogen-containing sites. Reusability was demonstrated over three adsorption–desorption cycles; however, removal efficiency declined from 95.10% to 61.65%, highlighting the need for improved regeneration. These findings demonstrate the potential of HM-CPF for Pb(II) and Hg(II) removal and underscore the contribution of accessible binding sites and mesoporosity to adsorption performance.

Keywords: Phosphazene-based covalent framework; Heavy metal adsorption; Lead and mercury removal; Microwave-assisted synthesis; Nitrogen-rich adsorption sites; Adsorption kinetics.

1. Introduction

Some 80 percent of the world's wastewater is released into the environment untreated every day, endangering human health and ecosystems. This has been exacerbated by the heavy use of chemicals in modern industries, which contaminates water systems to alarming levels [1, 2]. Consequently, the issue of water recycling has become a global concern, and conventional treatment systems are incapable of efficiently removing a large number of pollutants, such as hydrocarbons [3], heavy metal ions [4], pesticides [5], pharmaceutical compounds [6], plastic additives [7], and dyes and pigments [8, 9]. Owing to the non-biodegradability and high toxicity of heavy metals, their effective separation from wastewater has become a formidable environmental problem. The leading cause of heavy metal pollution is the discharge of ions (Cu^{2+}, Pb^{2+}, Zn^{2+} and Cd^{2+}) into water bodies, arising from mining, electronics, electroplating, and textile industries [10, 11].

Approaches to reducing these pollutants include advanced oxidation processes [12], electrochemical degradation [13], biodegradation [14], ozonation [15], ultrasonic degradation[16], and granular activated carbon filtration [17, 18]. Of these approaches, the method of removal by absorption mechanisms is preferred due to easier operational procedures and higher efficiency compared with other methods [19, 20]. Among them, adsorption-based and membrane-based technologies which utilize porous materials like activated carbon [21], zeolites [22], MOFs [23], cyclodextrins [24], POPs [25], CN [26], and COF [7, 27] have evolved as the most popular processes in industries for water treatment.

Novel nanoporous materials, such as covalent organic frameworks (COFs), are being actively investigated as appealing adsorbents for water pollutants, as they can overcome the disadvantages of current sorbents [28-32]. Motivated by their wide applications in adsorption, catalysis, energy storage etc., research on COFs has grown considerably since the first introduction of COFs in 2005 by Yaghi et al [29].

Covalent Organic Frameworks (COFs) are promising adsorbents with large surface areas, tunable pores and functional groups, which allow significant improvement of the adsorption for multiple contaminants. Recently, various studies have been focused on their rare ability to effectively sequester both heavy metals and organic pollutants from aqueous solutions through surface adsorption, chemical reactions, and electrostatic interactions. However, modifying the COF structure with electron-donating moieties considerably improves their ability to capture metal ions (now on par with MOFs). Furthermore, the structural stability of COFs in aqueous environments allows their long-term application in the field of water treatment [33-35]. These complexation behaviors align with acid-base theory — unpaired lone electron pairs on oxygen, nitrogen, or sulfur atoms can coordinate (bond) with metal ions. Hence, heavy metals ions like Pb2+, Cu2+, Zn2+, Hg2+ and Cd2+ can generate stable coordination complexes with negatively charged ligands such as O, P, N or S atoms, allowing their effective removal from aqueous solutions via chelation [36]. It has been recently reported that due to advancement in the technology of water purification these methods are capable of

removing large number of water pollutants [37]. When used in adsorption, COFs exhibit a high affinity toward adsorbing toxic heavy metals, and improve metal ion and organic pollutant removal rates as a result [33]. The structural formation of COFs is determined by reticular chemistry based on robust covalent linkages between monomers [38, 39].

Besides, functionalization like hydrogen bonding and π–π stacking could greatly increase the adsorption capacity of COFs for a wide range of pollutants, including heavy metals, dyes, and organic compounds [11]. The incorporation of phosphorus and nitrogen into the COF structure induces polarization within otherwise stable hydrogen bond systems, leading to the formation of new charged functional groups such as phosphate and amine [40-42]. Consequently, positive or negative charges can be incorporated into the system through COF structures, which can subsequently modulate the interactions of neutral or polar pollutants forming anchors with the system. The adsorption of oppositely charged pollutants, such as ions or polar molecules, to the charged areas of the COF structure is due only to electrostatic interactions [43, 44].

Since the first successful synthesis of COFs using solvothermal methods, researchers have developed several alternative synthesis approaches, including ionothermal synthesis [45-47], microwave heating [47-49], and the fabrication of monolayers or films via substrate-based reactions [32, 50]. Microwave heating is also used as a rapid method to enhance the synthesis of crystalline COF materials [38, 45]. In addition, microwave-assisted synthesis has additional benefits over conventional solvothermal methods since it permits more convenient and green synthesis of borate-linked COFs in a seed microwave reactor. The reaction time for microwave synthesis is much shorter, e.g., only 20 minutes for COF-5 and COF-102 obtained microwave [51, 52]. in contrast to the 72 h or longer for solvothermal synthesis. Method A, microwave-assisted synthesis, combined with solvent extraction, performed better in relation to the washing of residues and impurities, leading to a more porous final product. Further, despite the success of microwave-assisted synthesis, it still poses a major problem in scaling up COFs that exhibit high crystallinity and stability for production [49, 53-55].

Although significant advances have been made in the synthesis of COFs, they still lag behind their MOF counterparts, which predominantly exhibit crystalline structures but can also form amorphous frameworks with distinct properties. Amorphous organic frameworks retain the essential structural motifs and connectivity of their crystalline counterparts, even though they lack long-range periodicity. The lack of periodic atomic arrangements results in X-ray diffraction patterns with broad, featureless peaks due to diffuse scattering, making amorphous frameworks difficult to distinguish from one another [56]. A limited yet increasing number of noncrystalline COFs is gaining scientific attention; however, well-defined examples of amorphous COFs (aCOFs) have only recently been reported. The morphology of covalent organic frameworks (COFs) needs to be controlled to optimize their applications [56, 57].

Here, we develop a microwave-assisted approach for the synthesis of an amorphous covalent organic framework (aCOF), the phosphazene-triazine COF (HM-COF),

which is accomplished in a considerably shorter time than for conventional synthesis methods. Moreover, the porous structure and optimized surface characteristics of HM-COF were favorable for the adsorption of heavy metal ions and dyes from the aqueous phase. A novel hybrid porous structure was developed by simple microwave-assisted self-assembly of HM-COF from 1,3,5-triazine-2,4,6-trichloride (hexachloro-cyclo-trisphosphazene, HCCP) and 1,3,5-triazine-2,4,6-triamine (melamine, MA) monomers.

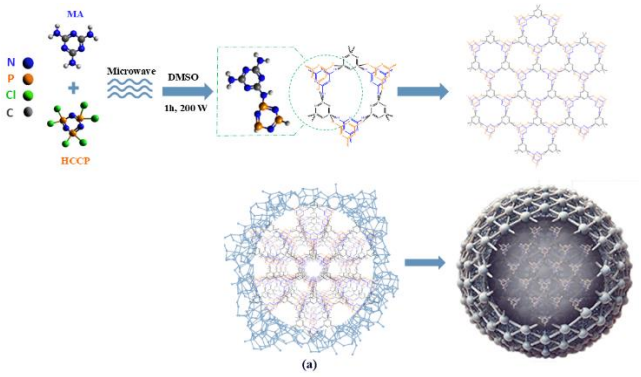

Scheme 1. Schematic representation of a HM-COF synthesis. (a) The HM-CPF framework possesses a crystalline core, although it lacks an organized structure beyond the center area.

2. Experimental

2.1. Materials

All chemicals were used as received without purification. MA was obtained from Sigma-Aldrich (Germany). Hexachloro phosphazene (HCP) was obtained from Sigma-Aldrich (Munich, Germany). The solvents (acetone, ethanol, dimethyl sulfoxide (DMSO), dimethyl formamide (DMF) and tetrahydrofuran (THF)) used were of analytical grade and were purchased from Merck (Darmstadt, Germany). Aqueous solutions were used for washing and purification of COFs as well as throughout the experiments. These solutions were prepared using double-distilled water. For pH adjustment, sodium hydroxide (NaOH) and hydrochloric acid (HCl) were acquired from Merck (Germany). The metal ion sources, all of analytical reagent grade (>99.0%), were also obtained from Merck (Germany), including: copper(II) nitrate ($Cu(NO_3)_2$), zinc(II) nitrate ($Zn(NO_3)_2$), lead(II) nitrate ($Pb(NO_3)_2$), cadmium(II) nitrate ($Cd(NO_3)_2$), mercury(II) nitrate monohydrate ($Hg(NO_3)_2 \cdot H_2O$), chromium(III) nitrate nonahydrate ($Cr(NO_3)_3 \cdot 9H_2O$), and arsenic acid (H_3AsO_4). All other chemicals were used as received without additional purification.

2.2. Material characterizations

FT-IR samples were prepared as KBr pellets. Scanning electron microscopy (SEM) images were obtained using an ULTRA Plus electron microscope (Zeiss, Germany). Specific surface area and pore structure were measured by nitrogen adsorption-desorption at 77 K using a Quantachrome Autosorb 1 (USA). Thermogravimetric analysis (TGA) was carried out on a TA Instruments TGA 55 (USA) by heating the samples from 25 °C to 800 °C at a heating rate of 10 °C·min^{-1} in the nitrogen or air atmosphere. Powder X-ray diffraction (PXRD) patterns of ST-COF-1 were measured on a BRUKER D8-Advance diffractometer using Cu Kα radiation (λ=1.5406 Å). Elemental analysis (EA) was performed using a Vario Micro Cube elemental analyzer (Elementar, Germany). Transmission electron microscopy (TEM) images were taken at a Tecnai G2 F30 (FEI Corp., Netherlands) microscope operating at 200 kV. Nitrogen adsorption-desorption isotherms were measured in a Micromeritics ASAP 2460 Surface Area and Porosity Analyzer. All samples were degassed for a minimum of 8 hours at 110 °C under 10^{-5} bar

vacuum prior to the analysis. Nitrogen adsorption-desorption isotherms were used to calculate the Brunauer–Emmett–Teller (BET) surface area. Then the t-plot method was employed to calculate the micropore surface area and volume from this data. The total pore volume was obtained from the nitrogen sorption isotherms at a relative pressure of P/P_0 = 0.995. The pore size distribution was obtained by applying the nonlocal density functional theory (NLDFT) model with a cylindrical pore geometry. CO_2 adsorption isotherms at 273 and 298 K (up to 1.13 bar relative pressure) were measured with Micromeritics ASAP 2020 Surface Area and Porosity Analyzer. High-pressure methane excess adsorption isotherms were measured in the pressure range of 0–100 bar at 273 and 298 K using a BELSORP-HP apparatus.

Reactions were conducted in a Milestone microwave reactor (North America) operating at 2.45 GHz. The reactor was designed to improve reaction efficiency and reduce processing time, with both temperature and power being uniformly monitored and controlled throughout the entire sample volume. The distribution of particle size was analyzed hydrodynamically using a HORIBA Scientific SZ-100 particle size analyzer. The scattering angle was fixed at 90°, and the temperature was maintained at 25.0 °C, with the viscosity of the dispersion medium being 0.896 mPa·s and the transmission intensity before measurement being 21,439. A monodisperse distribution was further confirmed by the light intensity data, as evidenced by the count rate of 667. Zeta potential measurements were obtained at 24.9 °C using a HORIBA Scientific SZ-100, with the dispersion medium having a viscosity of 0.897 mPa·s and conductivity of 0.201 mS/cm. An applied electrode voltage of 3.4 V was used, which is necessary to validate the stability of the colloidal dispersion. Atomic absorption spectroscopy (AAS) was performed using a Shimadzu AA-6880 instrument.

2.3. Preparation of HM-CPF

HM-CPF was synthesized via polycondensation reaction of hexachloro-cyclotriphosphazene (HCCP) with melamine in DMSO. In a standard synthesis, as shown in Scheme 1, 3.5 mmol of HCCP and 7.0 mmol of melamine monomers were first dissolved in 15 mL of DMSO by sonication for 30 minutes until all the monomers were dissolved completely. These solutions were then mixed in a Teflon-lined vessel that was sealed. A Milestone microwave reactor (North America) was used to heat the reaction mixture (200 W, 20 min) to encourage COF formation. The reaction period was followed by filtration of the solid product, which was then washed under sequentially with ethanol, DMF, acetone and excessive THF to ensure the removal of unreacted materials. For the purification of exosomes each wash step was centrifuged. The resulting powder was vacuum dried overnight at 60 °C. The obtained powder exhibited a milky-white color.

2.4. Adsorption studies

2.4.1. Kinetics of adsorption

Deionized water and standard solutions (1000 ppm) of Pb^{2+}, Cu^{2+}, Zn^{2+}, Hg^{2+}, Cd^{2+}, Cr^{3+}, and Ar^{3+} were used. To obtain the concentrations of these heavy metals (100-900 ppm), stock solutions were diluted with deionized water. Then 10 mg of adsorbent was added to each metal solution (20 mL).

The mixtures were sonicated at 25 °C for contact times ranging from 10 to 180 minutes. After adsorption, 5 mL of the solution containing the adsorbent was filtered, and the residual concentrations of heavy metals were measured using an Atomic Absorption Spectroscopy (AAS) instrument (Shimadzu AA-6880). The adsorption capacity (Qe, mg g^{-1}) was calculated according to Eq. (1):

$$Q_e = \frac{(C_0 - C_e)V}{m}$$

$$Q_t = \frac{(C_0 - C_t)V}{m}$$

Qe (mg g^{-1}) and Qt (mg g^{-1}) are the equilibrium adsorption capacity and the adsorption time, respectively. The initial concentration and the concentration at time t are represented by C_0 (mg g^{-1}) and C_t (mg g^{-1}), while C_e(mg g^{-1}) represents the equilibrium concentration. V (mL) is the volume of the water sample and m represents the mass of HM-COF in mg. The pseudo-first-order and pseudo-second-order kinetic models define the adsorption data:

$$\ln(Q_e - Q_t) = -k_1 t + Ina_e$$

$$\frac{t}{Q_t} = \frac{t}{Q_e} + \frac{1}{K_2 \times Q_e^2}$$

The rate constants for the pseudo-first-order and pseudo-second-order kinetic models are represented as k_1 (min^{-1}) and k_2 (g $mg^{-1}min^{-1}$), respectively.

2.4.2. Isothermal adsorption

To each 20 mL solution of one of the seven heavy metals, namely, Pb^{2+}, Cu^{2+}, Zn^{2+}, Hg^{2+}, Cd^{2+}, Cr^{3+}, and Ar^{3+}, 10 mg of HM-CPF was added, while the metal concentration varied from 50 to 900 mg L^{-1}. The mixtures were then subjected to ultrasonication for 30 hours at room temperature. The adsorption data were fitted into Freundlich and Langmuir equations as follows:

$$Q = \frac{k_L \times Q_m \times C_e}{1 \times k_L \times Ce}$$

$$Q_e = K_F \times C_e^{1/n} F$$

Where Q_m(mg g^{-1}) represents the maximum adsorption capacity, K_L(L mg^{-1}) denotes the adsorption constant in the Langmuir isotherm model, and n_F and k_f are the adsorption constants associated with the Freundlich isotherm model.

2.4.3. Selectivity

The selectivity of HM-CPF was evaluated using Pb2+, Cu2+, Zn2+, Hg2+, Cd2+, Cr3+, and Ar3+ ions. Each working solution (10 mL, 500 mg g^{-1}) was stirred with 10 mg of HM-CPF for 24 hours.

2.4.3. Reusability

10 mg of the adsorbent was added to 20 mL of each heavy metal solution, all with a concentration of 250 mol L^{-1}. Following a 24-hour adsorption period, the washing process was conducted using HNO_3 solution, and the eluted substance was then employed for further adsorption studies.

3. Results and discussions

3.1. FT-IR

Fig. 1 illustrates the FT-IR analysis, which proves the structure of HM-CPF was successfully formed. The significant spectral shifts between reactants HCCP and MA and the products show evidence of structural changes. The absorption bands at around 3417 and 2992 cm^{-1} are attributed to the stretching vibrations of H-N bonds [58, 59]. The peaks observed at 1556, 1489 and 1341

cm^{-1} can be assigned to triazine rings [60] , confirming this moiety incorporation. Moreover, the absorption bands at 1191 and 1156 cm^{-1} are ascribed to the P=N stretching vibrations of the cyclotriphosphazene moiety [61]. Characteristics associated with the stretching vibrations of P-NH–C at 1042 and 949 cm^{-1} also substantiate the successful polycondensation [62]. Collectively, these spectral features further confirm the successful synthesis and structural integrity of HM-CPF.

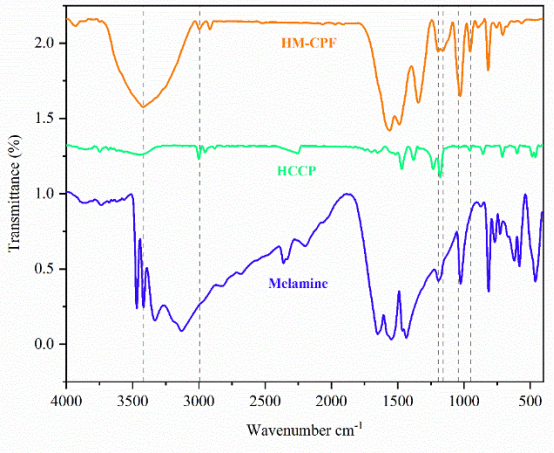

Figure.1 FTIR analysis of MA, HCCP and HM-CPF

3.2. TGA

As illustrated in Fig .2, thermogravimetric analysis (TGA) is an important method for the evaluation of the synthesized COF thermal stability. The negligible weight loss under 100 °C corresponds to the desorption of the chemisorbed water and the low-boiling-point solvent which typically resided in the micropores of porous materials derived from COFs. The first predominant thermal degradation process was observed between 100 °C and 330 °C, most probably due to the degradation of unreacted monomers and low-molecular-weight oligomers confined within the network. From 330 °C to 400 °C, an even greater mass loss occurs, which is primarily due to the partial breakage of the organic framework, especially degradation of the triazine rings and P=N bonds [61, 63]. This decomposition tendency is in line with prior works on triazine-containing COFs that showed thermal degradation behavior in the same manner. Above 400 °C, additional mass loss corresponds to carbonization, as well as the decomposition of any remaining aromatic structures [64]. These results demonstrate that the synthesized COF possesses good thermal stability until 330 °C, attributed to the rigidity of its covalent network. This thermal stability is on par with that of other triazine-based COFs and further demonstrates its structural robustness under harsh, high-temperature conditions.

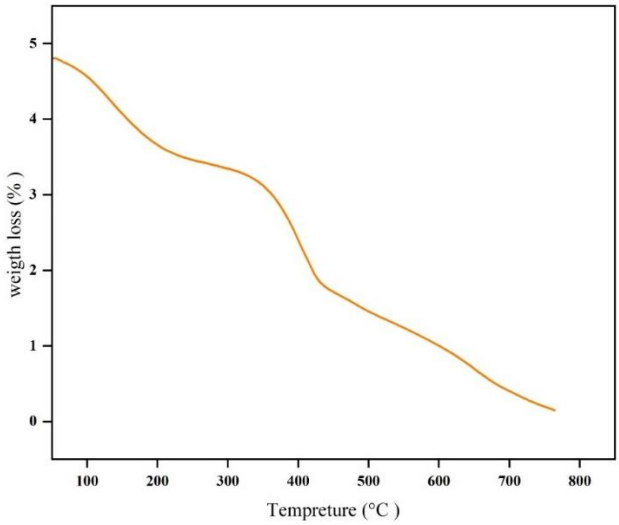

Figure.2 TGA curves under a N2 atmosphere of the HM-CPF

3.3. XRD

The synthesized COF is characterized by its XRD pattern. As indicated in Figure 3, in addition to the structural properties, the strong diffraction peak at 21.36° (2θ) corresponds to a d-spacing of 4.156 Å and is typical of two-dimensional COFs, suggesting the formation of layered structures. This peak, however, seems quite broadened, characterized by a Full Width at Half Maximum (FWHM) value of 7, pointing out

a reduced crystallite size window and/or some structural disorder inside the sample. The crystallite size is calculated using the Scherrer equation, which is 11.56 nm, confirming the nanocrystalline nature of COF. In addition, the semi-crystalline characteristic of the COF is involved in the formation of unique structural features. In fact, such ordered domains improve its surface area and nano-porosity, parameters that are the crux in an array of applications. Additionally, the appearance of secondary peaks between 40° and 50° substantiates the formation of these domains, which demonstrates that although the material exhibits some amorphous properties, its crystalline nature remains. The intensity decreases gradually as a function of the angle, without sharp and well-defined peaks, which indicates a high level of structural disorder. The XRD pattern is in good accordance with the literature on two-dimensional COFs, whose thickness reflection peaks are usually broad and similar in angular ranges and can always be classified as semi-crystalline. The observed but wide peaks suggest medium-range order within the structure, which can be advantageous for practical usages like adsorption or catalysis. The existence of these structural parameters and the width of the diffraction peaks as well as the medium-range ordered structure all confirm that the COFs obtained here are a semi-crystalline substance.

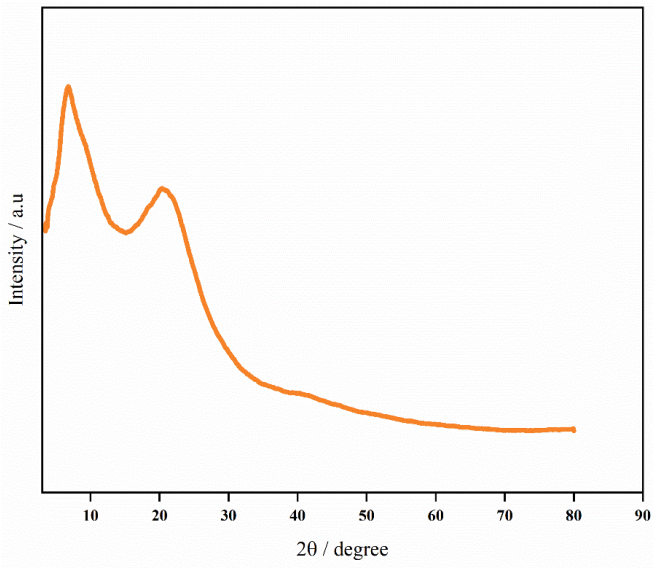

Figure.3 XRD patterns of the HM-CPF

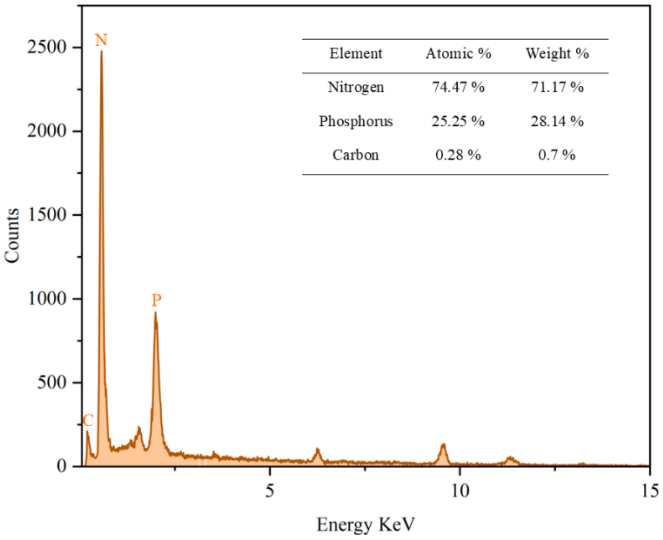

Figure 5. EDS analysis of HM-CPF

3.6. BET

The adsorption-desorption isotherms and pore size distribution of HM-CPF are illustrated in Fig.7 The isotherm's shape resembled the IUPAC-defined type IV isotherm. The hysteresis loop of the isotherms of HM-CPF exhibited characteristics type of H1 hysteresis as IUPAC categorization. The BET/BJH method reveals that the structural characteristics of the porous COF material include a surface area of 191.28 $m^2 g^{-1}$, a total

pore volume of 1.9185 $cm^3\ g^{-1}$, and a mean pore diameter of 10.65 nm. Moreover, the pore diameter determined by the BET/BJH technique are in agreement with the porous channel dimensions derived from the XRD study. The pore size distribution profile of the amorphous COF produced is wide and irregular, typical for amorphous materials with significant mesoporosity about 10 nm. Because there is no long-range order, a heterogeneous distribution can be obtained, supported by pore size variation between 1 and 100 nm. Based on this, dominant mesopores with some smaller micropores and occasional larger pores point toward amorphous structure. This is not surprising, because this is the nature of amorphous COFs. The random assembly usually has a wide spectrum of pore diameters, making the material potentially useful for application in adsorption or catalytic purposes. This analysis It proves that the synthesized COF exhibits semi-crystalline and amorphous features. This is well supported by a broad pore size distribution with the presence of ordered domains, such structural diversity enhancing its performance in adsorption and catalysis applications (Figure 8, Table 1).

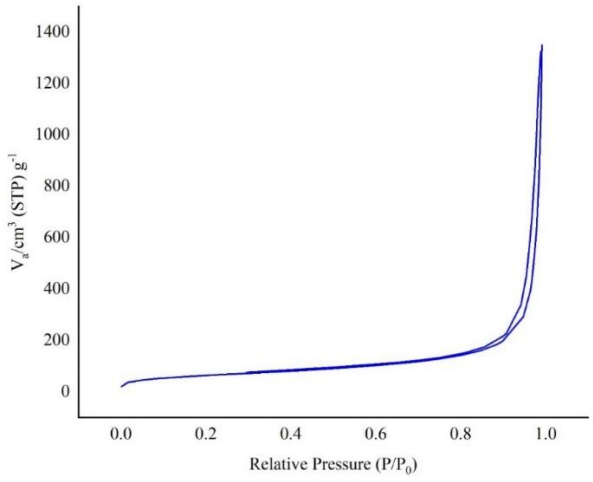

Figure.7 N_2 adsorption–desorption of HM-CPF

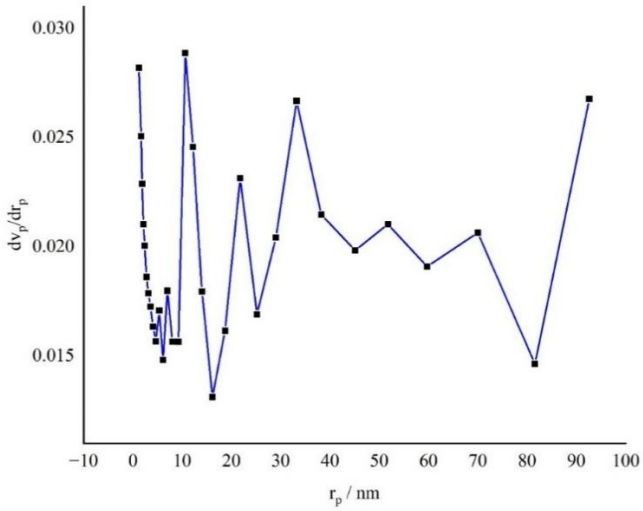

Figure.8 BJH pore size distribution of HM-CPF

Table 1. Specific surface area (S_{BET}), pore volume, mean pore diameter (BJH) of HM-CPF

Material	S_{BET} (m^2g^{-1})	Pore volume (cm^3g^{-1})	Mean pore diameter (nm)
HM-COF	191.28	1.9185	10.65

3.7. DLS and Zeta potential

The prepared COF was further analyzed for particle size distribution and colloidal stability by DLS and zeta potential analyses. A hydrodynamic diameter of 2554.5 nm and a polydispersity index (PI) of 1.017 were obtained by DLS measurement, confirming that the particles are polydispersed with a broad distribution in sizes. This is possibly because of the solvation layers or aggregation of the particles. In further analysis of particle size, the Gaussian fit of DLS data gave an average particle size of 500 nm ±1.00146 × 10^{-12} nm, while the width (FWHM) was 771.58 nm ±2.0785 × 10^{-12} nm. The latter fact is further proof of the quality of the fit, judged by the value of R^2 equal to 1, which can be considered as a robust description of the underlying particle size distribution. This zeta potential value of 18.3 mV refers to medium colloidal stability; it would be

speculated from this that the synthesized COF particles of this work are positive, hence preventing aggregation and promoting stability in aqueous solutions (Figure 9,10).

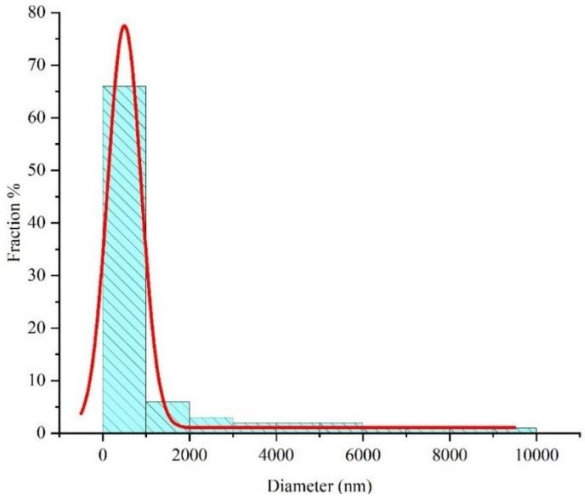

Figure 9. Particle size distribution of the synthesized HM-CPF as measured by DLS. The Gaussian fit indicates a mean particle size of 500 nm with a broad distribution (FWHM = 771.58 nm), reflecting the potential variability in particle dimensions.

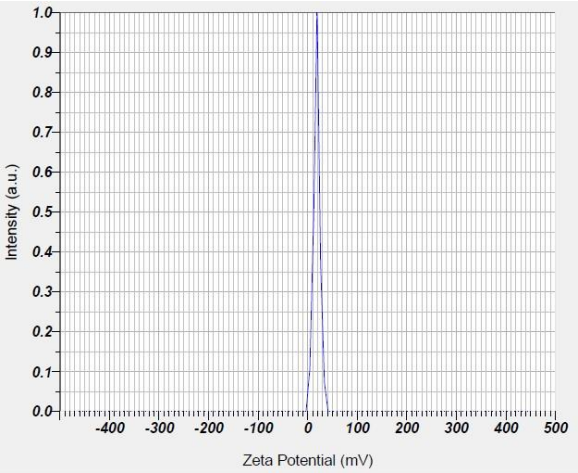

Figure 10. Zeta potential analysis of the synthesized HM-CPF, demonstrating a value of 18.3 mV, indicating moderate colloidal stability.

This large discrepancy between the DLS and 22 nm particle size from SEM underscores the use of multiple analysis techniques.

3.8. Adsorption experiments

3.8.1 Effect of pH

Figure 11 illustrates the effect of pH on removal efficiency for different heavy metal ions such as Cr^{3+}, As^{3+}, Zn^{2+}, Cd^{2+}, Cu^{2+}, Hg^{2+} and Pb^{2+}. Adsorption efficiency in general increases with the increase in pH values up to an optimum level then stabilizes or decreases depending on the metal ion. The Pb^{2+} ion exhibited the highest removal efficiency, reaching a maximum value of almost 100% at pH 5, after which it slightly decreased. These phenomena are understandable in that the adsorbent is effective in the capture of Pb^{2+} ions within the slightly acidic-neutral pH range, probably due to the alteration in the ion speciation and favorable electrostatic interactions. Similarly, Hg^{2+} showed high removal efficiency 80% at pH 5-6 and gradually decreased with further increase in pH; thus, this pH was indicated as the optimum adsorption condition. On the other hand, Cr^{3+}, As^{3+}, Zn^{2+}, Cd^{2+}, and Cu^{2+} ions exhibited removal efficiencies increasing moderately up to pH 5 and then mostly remaining constant or decreasing slightly. It is, therefore, possible that such behavior may originate from hydroxo complexes or precipitates formed at higher pH value, which reduce the amount of free metal ions available for adsorption. In most cases, the pH range for effective removal was found to lie between 4 and 6, whereas metals Pb^{2+} and Hg^{2+} exhibited the highest adsorption efficiency. All these findings are in implication that pH is the key and core in the optimization performance for the adsorbent in the removal of heavy metals from aqueous solutions.

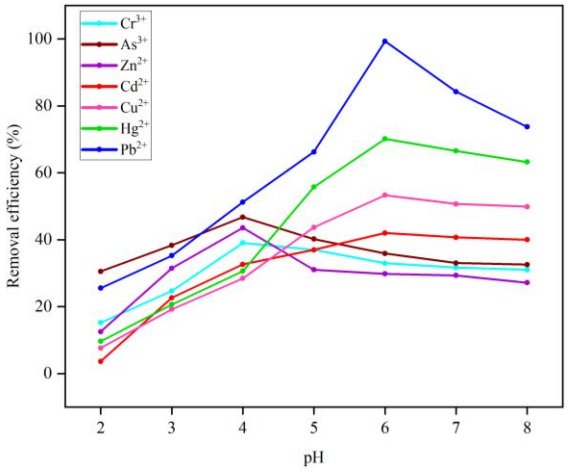

Figure 11. Effect of pH on the adsorption capacity of Pb^{2+}, Cu^{2+}, Zn^{2+}, Cd^{2+}, Hg^{2+}, As^{3+}, Cr^{3+} on HM-CPF

3.8.2. Adsorption kinetics

Fig. 12 illustrates the adsorption kinetics of various metal ions on HM-CPF were investigated using the pseudo-second-order kinetic model. The results demonstrated that Pb^{2+} exhibited the highest adsorption capacity ($q_e = 2834.91 mg.g^{-1}$) and the fastest adsorption rate ($k_2 = 2.5 \times 10^{-3}$) with an excellent model fit ($R^2 = 0.999$), indicating the highly efficient removal of lead ions. Hg^{2+} also showed a strong correlation to the pseudo-second-order model($R^2 = 0.988$) and a relatively high adsorption capacity ($q_e = 728.86\, mg.g^{-1}$), although its adsorption rate ($k_2 = 1.39 \times 10^{-4}$) was slower than that of Pb^{2+}. For Cu^{3+} and Cd^{2+}, the adsorption capacities were moderate ($q_e = 511.10\, mg.g^{-1}$ and $465.94\, mg.g^{-1}$, respectively), but their adsorption rates were significantly lower ($k_2 = 2.55 \times 10^{-5}$ and 3.1×10^{-5}, respectively), reflecting slower adsorption kinetics. In contrast, As^{2+}, Zn^{2+}, and Cr^{3+} exhibited lower adsorption capacities ($q_e = 351.19$, 322.82, and$104.57\, mg.g^{-1}$, respectively) and weaker correlation to the kinetic model, particularly for Zn^{2+} and, with R^2 values of 0.755 and 0.735, respectively. Although the adsorption rates for As^{2+}, Zn^{2+}, and Cr^{3+} ($k_2 = 9.98 \times 10^{-4}$, 8.14×10^{-4}, and 7.52×10^{-4})were somewhat higher than for Cu^{3+} and Cd^{2+}, the overall adsorption efficiency was notably lower. These findings highlight the superior performance of HM−CPF for the rapid and efficient removal of Pb^{2+}, while it shows relatively less effectiveness for other metal ions, particularly Zn^{2+} and Cr^{3+} (Table 3).

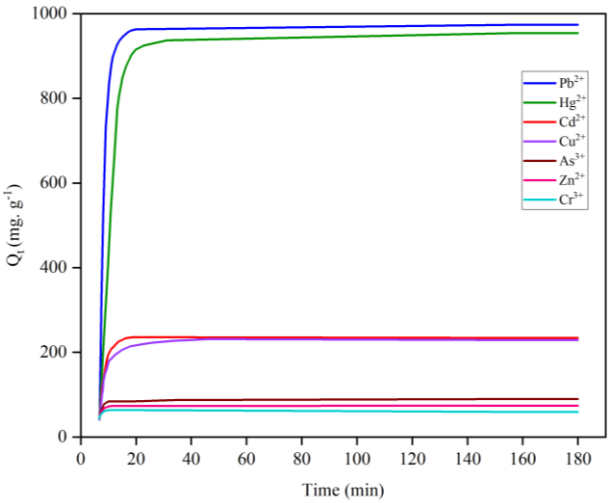

Figure 12. Adsorption kinetic curves of Pb^{2+}, Cu^{2+}, Zn^{2+}, Cd^{2+}, Hg^{2+}, As^{3+}, Cr^{3+} adsorption on HM-CPF

Table 3. Pseudo-second-order kinetic model parameters for the adsorption of Pb^{2+}, Cu^{2+}, Zn^{2+}, Cd^{2+}, Hg^{2+}, As^{3+}, Cr^{3+} on HM-CPF

Sample	R^2	K_2 (g/mg min)	q_{e2} (mg/g)
Pb^{2+}	0.999	2.5×10^{-3}	834.91
Hg^{2+}	0.988	1.39×10^{-4}	728.86
Cu^{2+}	0.935	2.55×10^{-5}	511.10
Cd^{2+}	0.951	3.1×10^{-5}	465.94
As^{3+}	0.841	9.98×10^{-4}	351.19
Zn^{2+}	0.755	8.14×10^{-4}	322.82
Cr^{3+}	0.735	7.52×10^{-4}	104.57

3.8.3. Adsorption isotherms

The adsorption capacities of heavy metals on HM-CPF can be evaluated using both the Langmuir and Freundlich isotherm models, as presented in the data of Fig. 13 and Fig. 14 and in Table 2. The Langmuir model indicates that Pb^{2+} exhibits the highest maximum adsorption capacity (q_m =982.2 mg/g) compared to other metals, such as Hg^{2+} (q_m =518.3 mg/g) and Cu^{2+} (q_m = 139.2 mg/g) This suggests that HM-CPF has a significantly higher affinity for lead ions, implying a potential preference in binding sites for Pb^{2+}. On the other hand, metals like Cr^{3+} and Zn^{2+} show relatively lower capacities (q_m = 98.54 mg/g and 104.33mg/g, respectively), indicating weaker adsorption interactions (Figure 11, Table 2).

In the Freundlich model, Pb^{2+} also shows strong adsorption affinity (with K_F =0.618mg/g and n_F =3.11mg/g) further supporting its dominance in binding compared to other metals. However, the Freundlich data suggest that the adsorption for metals such as As^{2+} and Cr^{3+} is less favorable, with lower K_F and n_F values. The results clearly highlight that HM-CPF is particularly efficient for Pb^{2+} removal, making it a promising material for treating lead-contaminated water, while its performance for other metals like Zn^{2+} and Cr^{3+} may require optimization (Figure 12, Table 2).

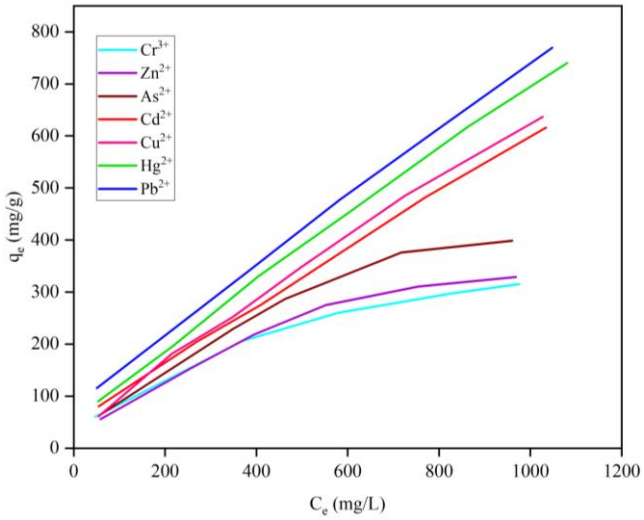

Figure 13. The Langmuir isotherm absorption model of Pb^{2+}, Cu^{2+}, Zn^{2+}, Cd^{2+}, Hg^{2+}, As^{2+}, Cr^{3+} on HM-CPF

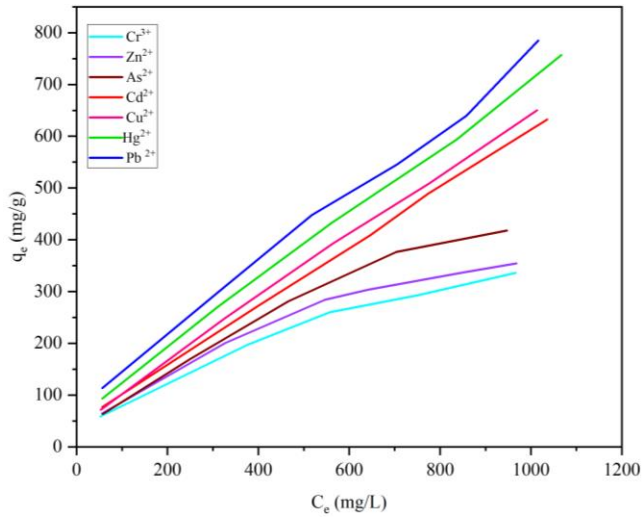

Figure 14. The Freundlich isotherm absorption model of Pb^{2+}, Cu^{2+}, Zn^{2+}, Cd^{2+}, Hg^{2+}, As^{2+}, Cr^{3+} on HM-CP

Table 2. Langmuir and Freundlich parameters for the adsorption of HM-CPF

Sample	Langmuir equation			Freundlich equation		
	R^2	K_L (L/mg)	q_m (mg/g)	R^2	K_F ((mg/g)/(mg/g)^n)	n_F
Pb^{2+}	0.9986	2.77×10-2	982.2	0.9807	6.18×10-1	3.11
Hg^{2+}	0.9809	1.79×10-2	518.3	0.9701	5.73×10-1	2.98
Cu^{2+}	0.9471	1.72×10-2	139.2	0.9302	5.001×10-1	2.59
Cd^{2+}	0.9401	1.53×10-2	124.7	0.9244	4.93×10-1	2.01
Zn^{2+}	0.9264	1.23×10-3	104.33	0.8832	3.14×10-1	1.19
As^{3+}	0.9424	1.13×10-4	201.01	0.8577	2.99×10-1	1.16
Cr^{3+}	0.9077	7.9×10-4	98.54	0.8207	1.66×10-1	1.008

3.8.4. Adsorbent selectivity

Competitive adsorption experiments with solutions containing seven ions [copper (Cu^{2+}), lead (Pb^{2+}), mercury (Hg^{2+}), zinc (Zn^{2+}), chromium (Cr^{3+}), cadmium (Cd^{2+}), and arsenic (As^{3+})] were conducted to observe the heavy metal loadability of HM-CPF. As shown in Figure 15 Tests revealed that the adsorption capacity of Hg^{2+} and Pb^{2+} was much higher than that of the competing ions, which were adsorbed in minute amounts. Therefore, because of the larger ionic radii and stronger coordination tendencies with Hg^{2+} and Pb^{2+}, the nitrogen and phosphorus groups interact more favorably, hence are bound together better. The negligible adsorption of Cu^{2+}, Zn^{2+}, Cr^{3+}, Cd^{2+}, and As^{3+} reveals a high selectivity of HM-CPF for the most toxic heavy metals: mercury and lead. The selectivity obtained is of great importance in different environmental applications, especially in the efficient removal of hazardous metals from aqueous systems (Fig. 15).

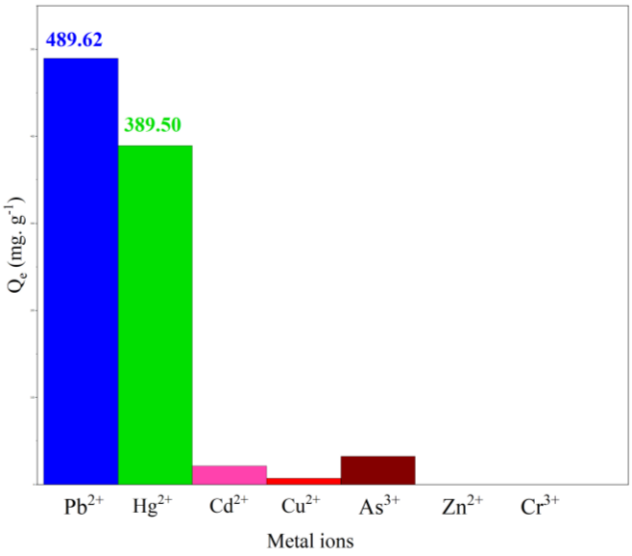

Figure 15. Selective adsorption of Pb^{2+}, Hg^{2+} by HM-CPF in the presence of Pb^{2+}, Cu^{2+}, Zn^{2+}, Cd^{2+}, Hg^{2+}, As^{3+}, and Cr^{3+}. The dosage of adsorbents, concentration, and contact time were 10 mg, 900 mg. g^{-1}, and 12 h, respectively.

3.8.5. Recycle performance

Fig. 16 illustrates the reusability of HM-CPT for the adsorption of Pb^{2+} and Hg^{2+} was evaluated during three successive adsorption-desorption cycles, demonstrating a progressive decrease in efficiency with each iteration. The initial adsorption efficiency was 95.10%, indicating a highly effective elimination of Pb^{2+} and Hg^{2+} ions. In the second cycle, however, the effectiveness decreased to 80.11%, either due to partial saturation of active sites or structural alterations in the material during regeneration. By the third cycle, the efficiency further decreased to 61.65%, indicating a noticeable reduction in performance. This tendency underscores the necessity of refining the regeneration process or altering the material to improve its reusability. Nevertheless, HM-CPT continues to be a potential reusable adsorbent, particularly in scenarios where minor reductions in adsorption efficiency are acceptable.

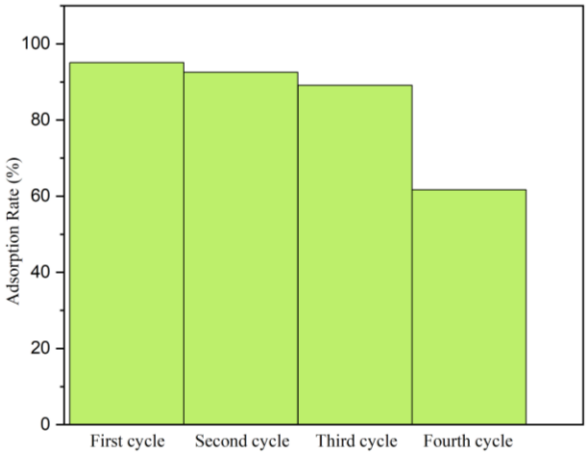

Figure 16. Reusability of HM-CPT for the adsorption of Pb2+ and Hg^{2+}

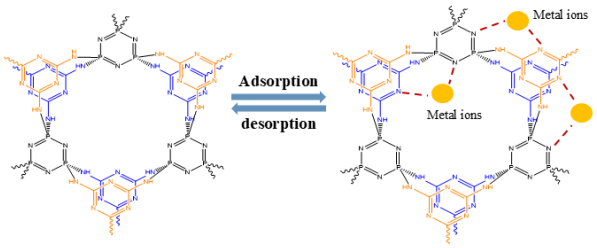

Scheme 2. Adsorption and desorption processes of heavy metal ions

The obtained HM-CPF possessed a unique combination of semi-crystalline and amorphous features that complement each other to enhance its adsorption efficiency and selectivity, as corroborated by complementary XRD and BET analyses. The XRD spectrum exhibited a sharp diffraction peak at 2θ = 21.36° with broad FWHM, typical of nanocrystalline domains embedded in a matrix lacking long-range order. This duality is further supported by BET measurements, which show a high specific surface area of 191.28 m^2/g representative for the semi-crystalline and amorphous framework. Above structure supports a diverse porosity profile with an average pore diameter estimated to be about 10.65 nm with a broad distribution into the mesopore and micropore regime. The consequence of this heterogeneous porosity allows a wide molecular size range to be adsorbed, which is thus advantageous in catalytic and environmental remediation applications.

Such a semi-crystalline and amorphous nature of HM-CPF allows for the synergistic combination of structural stability with high accessibility to adsorption sites. The pore size distribution is such that a maximum surface area is achieved to allow access to active sites that can accommodate larger-sized ions like Pb^{2+} and Hg^{2+}. This optimally provides a balance between stability and porosity, hence increasing the capacity of the material, more so towards large hazardous ions of higher affinity.

The larger hydrodynamic size in the case of DLS can be understood by including the solvation layers and also possible aggregation of particles, while SEM measures directly the real size of the particles. These results further confirm the unique structural feature of the synthesized HM-CPF and underpin its potential in environmental remediation and catalysis. All these findings together confirm the semi-amorphous and semi-crystalline nature of the HM-CPF and, in turn, point to its structural features responsible for adsorption and catalysis efficiency. The zeta potential measurements gave a moderately positive surface charge of +18.3 mV, and this is usually not good for adsorption of cationic metal ions because possible electrostatic repulsion may occur. However, in the actual experiment, the HM-CPF showed strong adsorption efficiency toward both Pb^{2+} and Hg^{2+}. The paradox can be explained by the existence of nitrogen and phosphorus functional groups inside the network within the HM-CPF framework that create localized negative charges. These negative sites now allow coordination interactions with the

metal ions to successfully offset the repulsive effects from the positive zeta potential. The nitrogen and phosphorus atoms also provide stable coordination bonds, hence providing chelation complexes with heavy metals, increasing the affinity and capacity of HM-CPF toward lead and mercury ions.

The ion size-polarizability relationship and competitive adsorption studies further supported the selectivity of HM-CPF toward Pb^{2+} and Hg^{2+}. The Pb^{2+} and Hg^{2+} ions, due to their relatively bigger ionic radii and high tendency for covalency in bonding, are well interacted with the nitrogen and phosphorus groups within the HM-CPF (Scheme 2). AS show in Table. 4, the results of some previous reports on heavy metal removal compared to the current study. In addition, the maximum adsorption capacity values for each adsorbent have been reported. As observed, the HM-CPF adsorbent showed a significant adsorption percentage for most metals and demonstrated excellent selectivity in removing mercury and lead. Further support for such selectivity could be obtained from Langmuir isotherm analysis, which showed that the maximum adsorption capacity of the HM-CPF was as high as 982.2 mg/g for Pb^{2+} and 518.3 mg/g for Hg^{2+}-far higher than that for the other metals-thereby underlining the efficiency of the HM-CPF in targeting these noxious contaminants. Such selective affinity also indicates the potential of this HM-CPF in environmental applications, such as the removal of certain heavy metals.

The kinetic studies also revealed that the nature of HM-CPF adsorption follows the pseudo-second-order model, while the rate of adsorption is high and reaches equilibrium within a time much smaller than that found for traditional adsorbents. The explanation is related to the mesoporous nature of the HM-CPF material that may support fast diffusions of the metal ions to reach the adsorption sites, and accessible functional groups within the framework also allow for further facilitation of this process. Therefore, high practical efficiency of HM-CPF in those applications where time is a factor has resulted.

4. Conclusions

In this respect, the synthesized HM-CPF is considered an advanced sorbent material in environmental remediation due to its superb combination of high surface area, manifold porosity, structural stability, and selective affinity towards heavy metals. The peculiar dual structure of HM-CPF facilitates its broad pore size distribution and maximizes the active site accessibilities, while functional groups allow targeted adsorption of Pb^{2+} and Hg^{2+} ions despite the moderate positive value of zeta potential. By comparison with all other covalent organic frameworks and nanoporous materials, this HM-CPF outperformed other materials in heavy metal sequestration and showed great promise for applications in water treatment with the goal of removal of highly toxic contaminants.

Conflicts of interest

The authors declare no competing interests.

Acknowledgements

Authors would like to thank Azarbaijan Shahid Madani University for the financial support.

References

1. Wang, R.-L., et al., *The preparation of new covalent organic framework embedded with silver nanoparticles and its applications in degradation of organic*

pollutants from waste water. Dalton Transactions, 2019. **48**(3): p. 1051-1059.
2. Jones, E.R., et al., *Country-level and gridded estimates of wastewater production, collection, treatment and reuse.* Earth System Science Data, 2021. **13**(2): p. 237-254.
3. Mohammadi, L., et al., *Petroleum hydrocarbon removal from wastewaters: a review.* Processes, 2020. **8**(4): p. 447.
4. Fu, F. and Q. Wang, *Removal of heavy metal ions from wastewaters: a review.* Journal of environmental management, 2011. **92**(3): p. 407-418.
5. Gan, J., et al., *Covalent organic frameworks-based smart materials for mitigation of pharmaceutical pollutants from aqueous solution.* Chemosphere, 2022. **286**: p. 131710.
6. Hao, M., et al., *Pyridinium salt-based covalent organic framework with well-defined nanochannels for efficient and selective capture of aqueous 99TcO4−.* Science bulletin, 2022. **67**(9): p. 924-932.
7. Wang, Z., et al., *Covalent organic frameworks for separation applications.* Chemical Society Reviews, 2020. **49**(3): p. 708-735.
8. Sun, J., et al., *Metal-organic frameworks and covalent organic frameworks as photocatalysts for H2O2 production from oxygen and water.* Journal of Materials Chemistry A, 2023.
9. Guo, L., et al., *Innovative Conversion Strategy for Wastewater with One-Pot Uranium Extraction and Valuable Chemical Production by a Smart COF Photocatalyst.* Advanced Functional Materials, 2024: p. 2400588.
10. Wang, H.Z., M.H.Y. Chan, and V.W.W. Yam, *Heavy-Metal Ions Removal and Iodine Capture by Terpyridine Covalent Organic Frameworks.* Small Methods, 2024: p. 2400465.
11. Da Silva, V., et al., *Covalent organic frameworks as promising materials for the removal of metal and organic pollutants from water.* Materials Today Sustainability, 2023. **21**: p. 100279.
12. Khan, J.A., et al., *Advanced oxidation processes for the treatment of contaminants of emerging concern*, in *Contaminants of emerging concern in water and wastewater*. 2020, Elsevier. p. 299-365.
13. Rafiee, M., et al., *COD Reduction of Aeration Effluent by Utilizing Optimum Quantities of UV/H2O2/O3 in a Small-Scale Reactor.* Processes, 2022. **10**(11): p. 2441.
14. Bai, Y., et al., *Differential crop yield responses to elevated CO2 attributed to varying biomass part stimulations: a meta-analysis.* Plant and Soil, 2024: p. 1-16.
15. Agustina, T.E., H.M. Ang, and V.K. Vareek, *A review of synergistic effect of photocatalysis and ozonation on wastewater treatment.* Journal of Photochemistry and Photobiology C: Photochemistry Reviews, 2005. **6**(4): p. 264-273.
16. Wang, N., et al., *Study and application status of ultrasound in organic wastewater treatment.* Sustainability, 2023. **15**(21): p. 15524.
17. Wang, J. and H. Chen, *Catalytic ozonation for water and wastewater treatment: Recent advances and perspective.* Science of the Total Environment, 2020. **704**: p. 135249.
18. Altmann, J., et al., *Combination of granular activated carbon adsorption and deep-bed filtration as a single advanced wastewater treatment step for organic micropollutant and phosphorus removal.* Water research, 2016. **92**: p. 131-139.
19. Bisbey, R.P. and W.R. Dichtel, *Covalent organic frameworks as a platform for multidimensional polymerization.* ACS central science, 2017. **3**(6): p. 533-543.

20. Gendy, E.A., et al., *A review on the adsorption mechanism of different organic contaminants by covalent organic framework (COF) from the aquatic environment.* Environmental Science and Pollution Research, 2022. **29**(22): p. 32566-32593.
21. Xu, X., et al., *Designing activated carbon and porous carbon nanofibers for insight into their differences in adsorption affinity mechanisms of VOCs.* Applied Surface Science, 2024. **659**: p. 159961.
22. Slavova, M., et al., *Application of zeolite and comparable porous materials for enhancing the performance of different types of secondary batteries: A review article.* Journal of Energy Storage, 2024. **98**: p. 112949.
23. Lee, G., et al., *Adsorptive removal of organic pollutants with a specific functional group from water by using metal–organic frameworks (MOFs) or MOF-derived carbons: A review.* Separation and Purification Technology, 2024: p. 127602.
24. Ismail, U.M., M.S. Vohra, and S.A. Onaizi, *Adsorptive removal of heavy metals from aqueous solutions: Progress of adsorbents development and their effectiveness.* Environmental Research, 2024: p. 118562.
25. Topuz, F., et al., *Advances in polymers of intrinsic microporosity (PIMs)-based materials for membrane, environmental, catalysis, sensing and energy applications.* Polymer Reviews, 2024. **64**(1): p. 251-305.
26. Bhanderi, D., P. Lakhani, and C.K. Modi, *Graphitic carbon nitride (gC 3 N 4) as an emerging photocatalyst for sustainable environmental applications: a comprehensive review.* RSC Sustainability, 2024.
27. Bagheri, A.R., et al., *Recent advances in the application of covalent organic frameworks in extraction: a review.* Critical Reviews in Analytical Chemistry, 2024. **54**(3): p. 565-598.
28. Vo, T.S., K.M. Lwin, and K. Kim, *Recent developments of nano-enhanced composite membranes designed for water/wastewater purification—a review.* Advanced Composites and Hybrid Materials, 2024. **7**(4): p. 1-38.
29. Guo, J. and D. Jiang, *Covalent organic frameworks for heterogeneous catalysis: principle, current status, and challenges.* ACS Central Science, 2020. **6**(6): p. 869-879.
30. Cote, A.P., et al., *Porous, crystalline, covalent organic frameworks.* science, 2005. **310**(5751): p. 1166-1170.
31. Beuerle, F. and B. Gole, *Covalent organic frameworks and cage compounds: design and applications of polymeric and discrete organic scaffolds.* Angewandte Chemie International Edition, 2018. **57**(18): p. 4850-4878.
32. Xue, S., et al., *Advanced development of three-dimensional covalent organic frameworks: Valency design, functionalization, and applications.* Coordination Chemistry Reviews, 2024. **504**: p. 215659.
33. Xia, Z., Y. Zhao, and S.B. Darling, *Covalent organic frameworks for water treatment.* Advanced Materials Interfaces, 2021. **8**(1): p. 2001507.
34. Liu, X., et al., *Advanced porous nanomaterials as superior adsorbents for environmental pollutants removal from aqueous solutions.* Critical Reviews in Environmental Science and Technology, 2023. **53**(13): p. 1289-1309.
35. Banjerdteerakul, K., H. Peng, and K. Li, *COF-based nanofiltration membrane for effective treatment of wastewater containing pharmaceutical residues.* Journal of Membrane Science, 2023. **681**: p. 121780.
36. Cao, Y., et al., *Sulfhydryl functionalized covalent organic framework as an efficient adsorbent for selective Pb (II)*

removal. Colloids and Surfaces A: Physicochemical and Engineering Aspects, 2020. **600**: p. 125004.
37. Khan, N.A., et al., *Structural characteristics and environmental applications of covalent organic frameworks.* Energies, 2021. **14**(8): p. 2267.
38. Geng, K., et al., *Covalent organic frameworks: design, synthesis, and functions.* Chemical reviews, 2020. **120**(16): p. 8814-8933.
39. Xue, R., et al., *A novel microporous phosphazene-triazinyl based covalent organic framework: Preparation, characterization and fluorescence properties.* Optik, 2021. **242**: p. 167184.
40. Li, Z., et al., *Synergistic effects between doped nitrogen and phosphorus in metal-free cathode for zinc-air battery from covalent organic frameworks coated CNT.* ACS applied materials & interfaces, 2017. **9**(51): p. 44519-44528.
41. Wang, C., et al., *Harnessing the clean energy: Phosphorus-alkynyl covalent organic frameworks for photocatalytic hydrogen production.* International Journal of Hydrogen Energy, 2024. **86**: p. 293-299.
42. Ou, L., et al., *Nitrogen-containing linkage-bonds in covalent organic frameworks: Synthesis and applications.* Chinese Chemical Letters, 2024: p. 110294.
43. Romero, V., et al., *Efficient adsorption of endocrine-disrupting pesticides from water with a reusable magnetic covalent organic framework.* Microporous and Mesoporous Materials, 2020. **307**: p. 110523.
44. Zhong, X., et al., *The magnetic covalent organic framework as a platform for high-performance extraction of Cr (VI) and bisphenol a from aqueous solution.* Journal of hazardous materials, 2020. **393**: p. 122353.
45. Li, Y., et al., *New synthetic strategies toward covalent organic frameworks.* Chemical Society Reviews, 2020. **49**(10): p. 2852-2868.
46. Kuecken, S., et al., *Conversion of amorphous polymer networks to covalent organic frameworks under ionothermal conditions: A facile synthesis route for covalent triazine frameworks.* Journal of Materials Chemistry A, 2015. **3**(48): p. 24422-24427.
47. Kuhn, P., M. Antonietti, and A. Thomas, *Porous, covalent triazine-based frameworks prepared by ionothermal synthesis.* Angewandte Chemie International Edition, 2008. **47**(18): p. 3450-3453.
48. Campbell, N.L., et al., *Rapid microwave synthesis and purification of porous covalent organic frameworks.* Chemistry of Materials, 2009. **21**(2): p. 204-206.
49. Zhang, W., et al., *Microwave-enhanced synthesis of magnetic porous covalent triazine-based framework composites for fast separation of organic dye from aqueous solution.* Journal of Hazardous materials, 2011. **186**(2-3): p. 984-990.
50. Cao, S., et al., *Design and synthesis of covalent organic frameworks towards energy and environment fields.* Chemical Engineering Journal, 2019. **355**: p. 602-623.
51. Diaz de Grenu, B., et al., *Microwave-Assisted Synthesis of Covalent Organic Frameworks: A Review.* ChemSusChem, 2021. **14**(1): p. 208-233.
52. Kaur, H., et al., *Covalent–Organic Framework-Based Materials in Theranostic Applications: Insights into Their Advantages and Challenges.* ACS omega, 2024. **9**(6): p. 6235-6252.
53. Alsudairy, Z., et al., *Microwave-assisted synthesis of mixed-linker covalent organic frameworks enabling tunable and ultrahigh iodine capture.* Chemical Engineering Journal, 2024. **485**: p. 149135.

54. Lavillunière, H., et al., *Controlled Microwave-Assisted Synthesis of Covalent Organic Frameworks Opens the Way Toward More Suitable Porous Supercapacitor Electrodes.* ACS Applied Energy Materials, 2024. **7**(5): p. 1723-1734.
55. Sabzi, F.E., et al., *Bifunctional PEI@ MSN@ COP nanohybrid for efficient adsorption and fluorescence sensing of mercury (II) in water.* Environmental Science and Pollution Research, 2026: p. 1-22.
56. Xiong, Z., et al., *Amorphous-to-crystalline transformation: General synthesis of hollow structured covalent organic frameworks with high crystallinity.* Journal of the American Chemical Society, 2022. **144**(14): p. 6583-6593.
57. Sabzi, F.E., et al., *Selective dye removal from real wastewater using a microwave-assisted triazine-phosphazene COF: mechanistic insights and recyclability.* Water, Air, & Soil Pollution, 2026. **237**(13): p. 738.
58. Xue, R., et al., *A novel 2D mesoporous phosphazene-anthraquinone-based covalent organic polymer: synthesis, characterization and supercapacitor applications.* New Journal of Chemistry, 2021. **45**(40): p. 19125-19131.
59. Zhang, S., et al., *"Stereoscopic" 2D super-microporous phosphazene-based covalent organic framework: design, synthesis and selective sorption towards uranium at high acidic condition.* Journal of hazardous materials, 2016. **314**: p. 95-104.
60. Venkatesh, N., et al., *A novel nanocomposite based on Triazine based covalent organic polymer blended with porous g-C3N4 for photo catalytic dye degradation of rose Bengal and fast green.* Molecules, 2022. **27**(21): p. 7168.
61. Yu, Y., et al., *Synthesis of a Novel P/N-Triazine-Containing Ring Flame Retardant and Its Application in Epoxy Resin.* Polymers, 2024. **16**(7): p. 871.
62. Malkappa, K. and S.S. Ray, *Thermal stability, pyrolysis behavior, and fire-retardant performance of melamine cyanurate@ poly (cyclotriphosphazene-co-4, 4'-sulfonyl diphenol) hybrid nanosheet-containing polyamide 6 composites.* Acs Omega, 2019. **4**(6): p. 9615-9628.
63. Bagheri, A.R. and N. Aramesh, *Towards the room-temperature synthesis of covalent organic frameworks: a mini-review.* Journal of Materials Science, 2021. **56**(2): p. 1116-1132.
64. Vargheese, S., et al., *Triazine-based 2D covalent organic framework-derived nitrogen-doped porous carbon for supercapacitor electrode.* Carbon Letters, 2021. **31**: p. 879-886.
65. Jiang, Y., C. Liu, and A. Huang, *EDTA-functionalized covalent organic framework for the removal of heavy-metal ions.* ACS applied materials & interfaces, 2019. **11**(35): p. 32186-32191.
66. Huang, N., et al., *Stable covalent organic frameworks for exceptional mercury removal from aqueous solutions.* Journal of the American Chemical Society, 2017. **139**(6): p. 2428-2434.
67. Li, Y., et al., *Fabrication of hydrazone-linked covalent organic frameworks using alkyl amine as building block for high adsorption capacity of metal ions.* ACS applied materials & interfaces, 2019. **11**(12): p. 11706-11714.